ORIGINAL RESEARCH ARTICLE

Influence of Sintering Conditions on Anisotropy of Grain Boundary Networks and Microstructure Topology in Yttria-Stabilized Zirconia

MAREK FARYNA, KRZYSZTOF GŁOWIŃSKI, ROBERT CHULIST, and ZBIGNIEW PĘDZICH

The paper presents original data of 3D EBSD orientation maps collected for 13 Yttria-Stabilized Zirconia (YSG) samples, sintered at different temperatures for different times. The largest map contains 18,833 grains and 64,506 grain boundaries. These data allowed for the analysis of grain boundary networks, based on all 5 macroscopic parameters and some topological studies of microstructures. Grain boundaries having the (001) and (111) boundary planes are favored and disfavored respectfully in all YSZ samples. The anisotropy appears to be stronger if grains are larger. However, large grains themselves do not imply strong anisotropy. Symmetric boundaries are slightly more frequent in YSZ compared to random boundaries, but despite some premises, the evidence for over-representation of 180 deg-tilt boundaries is still too weak. Distributions of the number of faces per grain and mean number of faces per grain are similar to those reported for metals, and there is a close-to-linear correlation between the number of faces and grain size.

MAREK FARYNA, KRZYSZTOF GŁOWIŃSKI, and ROBERT CHULIST are with the Polish Academy of Sciences, Institute of Metallurgy and Materials Science, 25 Reymonta St., 30-059 Kraków, Poland. Contact e-mail: m.faryna@imim.pl ZBIGNIEW PĘDZICH is with the AGH-University of Science and Technology, Faculty of Materials Engineering and Ceramics, 30 Mickiewicza Av., 30-060 Kraków, Poland.

Manuscript submitted April 18, 2023; accepted August 8, 2023.
Article published online September 1, 2023

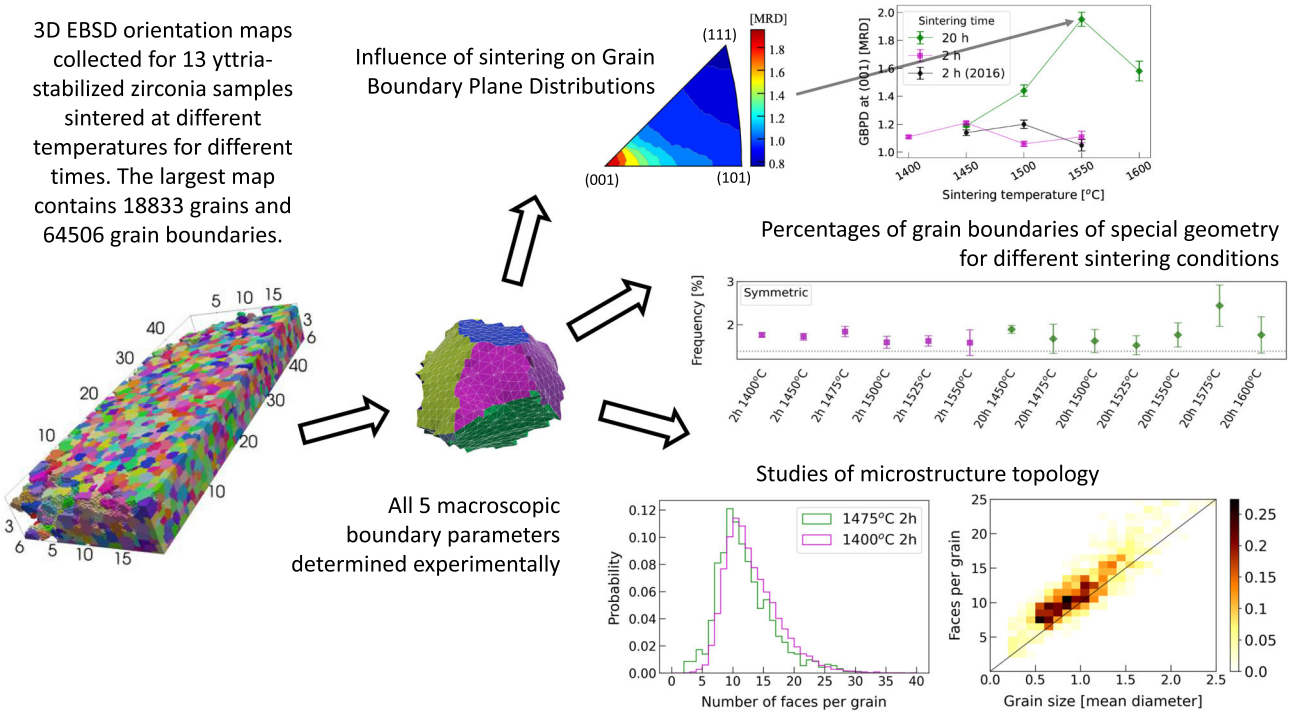

https://doi.org/10.1007/s11661-023-07171-0

I. INTRODUCTION

ZIRCONIA-BASED ceramics (ZrO_2) comprise a wide range of engineering materials with attractive mechanical, chemical and physical properties. These properties vary significantly depending on crystallographic structure and microstructure. For example, pure monoclinic ZrO_2 is an electronic insulator with poor mechanical properties, while tetragonal and cubic phases are characterized by very good mechanical properties and high ionic conductivity, compared to other ceramic materials. At room temperature, the tetragonal phase (t-ZrO_2) reveals superior mechanical properties, such as fracture toughness and wear resistance, which results from the phase transition from tetragonal to monoclinic structure, when the energy of cracks propagating within the material is being absorbed. The cubic phase (c-ZrO_2) is characterized by a very high value of oxygen ions conductivity at elevated temperatures, while being still an electronic insulator. This property makes the c-ZrO_2 an attractive material for application in solid oxide fuel cells (SOFCs), designed to replace internal combustion engines in the automotive industry and portable power devices.[1–4]

The polymorphic nature of pure zirconia is well known. High-temperature cubic phase (space group *Fm3m*) is stable from the melting point 2680 °C to 2370 °C. Between 2370 °C and 1170 °C, the tetragonal phase (space group $P4_2/nmc$) is present. Below 1170 °C, a further distortion to monoclinic symmetry (space group $P2_1/c$) occurs.[5,6]

High-temperature phases of zirconia, *i.e.,* cubic and tetragonal can be stabilized at room temperature by an addition of a few mol pct of oxides such as Ce_2O_3, MgO, CaO, or Y_2O_3. The addition of Yttria results in the most significant improvement of the oxygen conductivity among the mentioned oxides.[7] An addition of 2 mol pct of yttrium oxide enables the partial stabilization of the cubic phase at room temperature. Further increase of the Y_2O_3 concentration leads to the increase in the amount of the cubic phase present in the material. Additionally, the ionic conductivity raises along with the amount of dopant and reaches maximum value at about 8 mol pct. At higher dopant concentrations, the ionic conductivity begins to decrease. Based on this phenomenon, the zirconia with the addition of 8 mol pct of Yttria (often abbreviated as 8YSZ) is the most widely studied composition of cubic ZrO_2 with possible application as an ionic conductor.

Due to its intrinsic properties, the c-ZrO_2 is used as the main constituent of solid oxide fuel cells (SOFCs). All the main components of a typical fuel cell, namely, cathode, anode, and solid electrolyte, contain the c-ZrO_2, however, with various microstructures. The solid electrolyte is manufactured as a thin membrane composed of a dense c-ZrO_2 and is placed between the

anode and the cathode. It is supposed to separate reaction gases (such as O_2, H_2, H_2O or methanol) present within electrodes as well as to impede the flow of the electronic current; however, it should still conduct the oxygen ions. The cathode and the anode are manufactured from a composite material containing porous ZrO_2 and metallic particles.[8] The most frequently used metals are Ni, Ni-Fe, and Pt. In such a composite, all three phases should form continuous networks within the material allowing the flow of electrons, reaction gases, and oxygen ions through the metal, voids, and the ceramic, respectively. Due to the complexity of the structure, its proper characterization is required including information about particle and pore sizes, shapes, their interfaces, and mutual connectivity. Some of these microstructural parameters can be evaluated only by use of three-dimensional analysis techniques, which will be discussed later.

It is well known that features of engineering materials are impacted by their microstructure. This includes, but is not limited to, grain faces. Discontinuities of crystal structures between neighboring grains are referred to as grain boundaries and, from the crystallographic point of view, they are described by five so-called macroscopic boundary parameters. Three of them represent how the structures of abutting crystallites are rotated with respect to each other. The remaining two, *i.e.*, boundary plane parameters, specify Miller indices of crystallographic planes at grain faces.

With evolving possibilities of obtaining three-dimensional (3D) images of microstructures, and hence, of determining boundary plane parameters experimentally, there has been an increasing interest in quantitative studies of grain boundaries, also in zirconia. The first 3D orientation map for YSZ was obtained by Helmick.[9] Those data were used for computing the Grain Boundary Plane Distribution (GBPD) showing populations of grain boundaries as a function of their plane parameters. The distribution revealed that boundaries with grains terminated by (001) planes are mildly preferred in YSZ compared to random boundaries. The value of the GBPD at (001) reached about 1.2 MRD—Multiples of the Random Distribution. On the other hand, boundaries with (111) planes were disfavored. Then GBPDs were obtained based on 3D orientation maps collected for 3 YSZ samples sintered for 2 hours at 3 different temperatures: 1450 °C, 1500 °C, and 1550 °C.[10] The authors expected to see a relationship between the anisotropy and the sintering temperature. Although mild anisotropy was observed for the first two samples, the evidence for preference of (100) planes in the third sample was poor. Another aspect notified in Reference 10 was the estimation of (area-)fractions of grain boundaries of characteristic geometry, like symmetric, twist, and 180 deg-tilt grain boundaries. The outcome was some indication that symmetric and 180 deg-tilt boundaries might be slightly over-represented in the YSZ compared to random boundaries, but the statistical reliability of the data was insufficient to draw convincing conclusions.

In this work, we pursue investigating the above two topics: a potential relationship between anisotropy and material processing and the percentages of characteristic grain boundaries in the YSZ. For this purpose, more data were needed. Utilizing the 3D electron-backscatter diffraction (EBSD) technique, 3D orientation maps were collected from 13 different YSZ samples. These samples varied by their sintering time: either 2 or 20 hours, as well as sintering temperatures, ranging from 1400 °C to 1600 °C with 25 °C intervals. To the best of our knowledge, this is the biggest and the most diverse data source of grain boundary parameters collected so far for zirconia. Moreover, the largest of the obtained datasets (for the material sintered for 2 hours at 1400 °C) contains macroscopic parameters of as many as 64506 distinct grain boundaries, and it is probably the largest dataset with boundary parameters gathered ever for the YSZ.

For all the samples, we computed the GBPDs using the state-of-the-art approach based on Kernel Density Estimation (KDE).[11] The reliability of all the resulting distributions was meticulously assessed and cross-validated. We did observe stronger anisotropy, up to 2 MRD, for certain samples. Conditions for the increased anisotropy are discussed. Afterwards, the frequencies of occurrence of symmetric, twist, and 180 deg-tilt boundaries in each sample are calculated and reviewed. The aforementioned analyses are also interesting in the context of putting the concept of Grain Boundary Engineering[12] into practice. Since it is believed that grain boundary networks could be designed and introduced to materials in the desired form, some quantitative characteristics (covering whole boundary networks) would be needed for monitoring whether the manufacture of a given material succeeded. Both the GBPD and the fractions of geometrically special boundaries might be such characteristics. We take advantage of having access to data for sinters that underwent such a variety of processing, and explore how responsive these characteristics are to variations in material's processing.

In the further part, crystallographic studies of grain faces are supplemented by basic topological analysis of the microstructure. In particular, distributions of the number of faces per grain are presented along with the mean and maximum number of facets per crystallite. These parameters, obtained for zirconia, are then compared to the analogous results obtained in the past for metals.[13–17] The grain boundary analysis is also discussed with respect to the global texture which was measured in transmission geometry with high-energy synchrotron radiation to ensure good grain statistics.

As a side remark, it is worth mentioning that the collected data allowed for computing the 5D distributions showing populations of grain boundaries as functions of their 5 macroscopic parameters, but this is a vast topic which was thoroughly described in a separate study.[18]

II. EXPERIMENTAL PROCEDURE

A set of 14 samples manufactured from zirconia doped with 8 pct Yttria were prepared by calcination of co-precipitated hydroxides at 500 °C. The powders of specific surface area $S_w = 70.8 \pm 0.2$ m^2/g were

uniaxially compacted under the pressure of 50 MPa and consequently isostatically re-pressed under 350 MPa. Compacted samples were pressureless sintered at the following temperatures of 1400 °C, 1450 °C, 1475 °C, 1500 °C, 1550 °C, 1575 °C, and 1600 °C. Two soaking times were chosen, namely 2 and 20 hours for each temperature. Based on such a procedure, 14 cylindrical samples of 6 mm diameter and 1 mm thickness were prepared. Samples were denoted with a number according to the maximum temperature at which they were sintered and their soaking time. In order to determine whether any crystallographic texture appears during sintering of zirconia samples, the X-ray diffraction (XRD) measurements were carried out using the HZG beamline (P07B) located at PETRA III (electro-storage ring operating at energy 6 GeV with beam current 100 mA) at DESY, Hamburg, Germany. The high energy of synchrotron radiation (87.1 keV, $\lambda = 0.142342$ Å) allowed phase and texture analysis in transmission geometry.[19,20] Texture measurements were done by diffraction of synchrotron radiation with the beam size (1 × 1) mm^2, sample detector distance 1320 mm, and MarView flat panel detector with a pixel size of 150 μm. The orientation distribution function (ODF) was calculated from the measured (111), (200), and (220), pole figures (cubic phase) using LaboTex V3 software.[21] Measurements performed in transmission mode on bulk samples allowed the construction of complete pole figures in a single experiment. The Euler angles given are in the Bunge convention for orientation[22] with sample reference systems chosen arbitrarily. It should be stated that all X-rayed samples were composed exclusively from cubic zirconia phase.

Three-dimensional local crystallographic orientations for all samples were acquired in high vacuum conditions using the EDAX Hikari Super camera with pixel resolution 640(H)x480(W) based on a series of two-dimensional electron backscattered (EBSD) maps. Prior to 3D EBSD measurements, all compacted cylindrical samples were sputter coated with gold to obtain a continuous, thick, and conductive layer. The operating parameters of the electron beam were as follows: the accelerating voltage was set to 20 kV and the beam current to 11 nA. Diffraction patterns were analyzed at the rate of above 100 patterns per second. During 3D EBSD data acquisition the material was milled away using 30 kV and 5 nA beam of Ga^+ ions. Ion milling enabled the preparation of cross sections of high quality with smooth surfaces appropriate for EBSD measurements; however, it resulted also in removing Au conductive layer from the analyzed area. This was the reason why EBSD data were collected at relatively high rates, *i.e.*, above 100 frames per second. For all samples, the 3D EBSD maps were 50 μm wide and 25 μm high with 200 nm step size in both directions. Milling was performed 15 to 20 μm deep into the material with 200 nm slice thickness, which resulted in acquisition of 75-100 EBSD maps for each measurement. Values of the in-plane step size and the slice thickness were the same, *i.e.,* 200 nm, yielding undistorted cubic data voxels.

A. *Reconstruction*

3D orientation maps were reconstructed from the stacks of 2D EBSD maps collected at subsequent depths between successive removal of layers of the material. This reconstruction was carried out with the DREAM.3D program.[23] First, each stack of maps was aligned and cropped. In order to maximize the volume of data, some of the stacks were divided into 2 or 3 sub-stacks containing smaller numbers of slices. This additional step was introduced when the alignment shift between the topmost and the bottommost layers would be too large and would result in data loss. A couple of standard clean-up methods were also applied. Then, grains were reconstructed from clusters of at least 20 voxels whose associated orientations differed by at most 5°. Grains that would be entirely hidden inside another grain, *i.e.*, those neighboring with one grain only, were "eaten" by the surrounding grain. Later on, the grains were dilated. However, since the materials had some pores (and thus, non-indexed areas visible on the maps), 2 to 3 iterations only were used. This method eliminated random voxels of poor measurement confidence, without introducing artifacts to the data. Examples of final 3D maps are shown in Figure 1. From such maps, grain boundaries were reconstructed as networks of surfaces composed of flat triangular segments (for illustration, see Figure 1(e)). For each "triangle," the associated so-called macroscopic boundary parameters were derived: a vector normal to the segment can be easily determined, whereas misorientations between abutting grains were computed as differences in average orientations of the neighboring grains. In the analyses below, the outer surfaces and grain-pore surfaces were not taken into account. Only the boundaries separating crystallites are of interest. The numbers of grains and distinct grain boundaries (not triangular bricks), as well as mean grain sizes, for all obtained datasets, are collected in Table I.

III. RESULTS

The geometry of a grain boundary is described by five independent macroscopic boundary parameters. In a common representation, three of them are encapsulated by a misorientation matrix M while the remaining two—by a vector m_1 normal to the boundary plane.[25] With m_1 expressed in the coordinate frame attached to the 'first' grain, the components of the normal in the reference frame of the 'second' crystallite can be derived as $\mathrm{m}_2 = -M^T\mathrm{m}_1$. Due to crystal symmetries, a given physical boundary can be described by numerous equivalent sets of parameters, namely $M' = C_1 M C_2^T$, $\mathrm{m}'_1 = C_1\mathrm{m}_1$, and $\mathrm{m}'_2 = C_2\mathrm{m}_2$, with C_1 and C_2 being symmetry operators applied to the first and second grains, respectively. In the presence of the inversion (grain-interchange) symmetry, the description by the pair M and $-\mathrm{m}_1$ (M^T and m_2) is also equivalent to that by M and m_1.

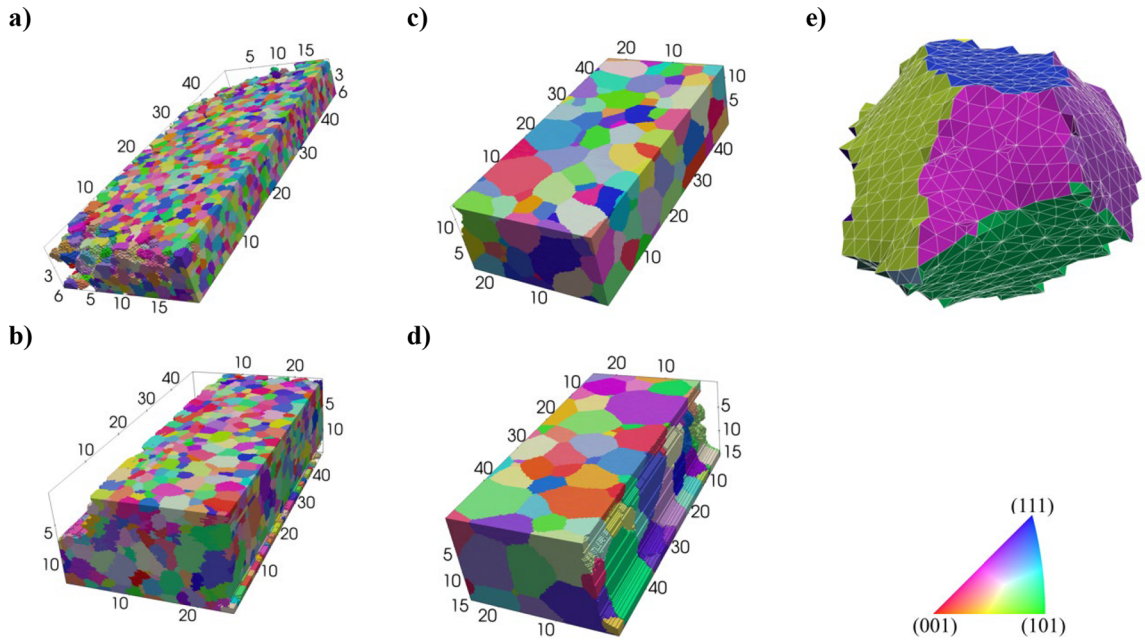

Fig. 1—(*a* through *d*) Examples of three-dimensional orientation maps after complete post-processing. Maps were collected from (a) *1400 °C-2 h-1a*, (b) *1450 °C-2 h-3*, (c) *1525 °C-20 h-5*, and (d) *1500 °C-20 h-3* datasets (cf. Table I). Colors correspond to the inverse pole figure (bottom right). Dimensions of the samples are given in μ m. (*e*) Mesh segments of the reconstructed boundaries for a selected grain from *1450C-2 h-3*. Diameter of this grain is 2.7 μ m. Visualizations were created using ParaView (Color figure online).[24]

One of the tools for analyzing grain boundary networks is distribution showing the frequencies of occurrence of boundaries as functions of their macroscopic parameters, from trivial disorientation angle distributions to five-dimensional functions with all 5 degrees of freedom included. One of the goals of collecting 3D orientation maps was to gather boundary plane parameters. Such data allow for obtaining distributions of boundary planes and the 5-parameter boundary distributions. As has already been mentioned, the latter are a broad topic which have been covered in a separate study.[18] In this paper, more attention is paid to grain boundary plane parameters independent of grain misorientations and to the 2-dimensional Grain Boundary Plane Distributions (GBPDs).

The distributions presented here were computed using the approach based on kernel density estimation.[11] In this technique, a distribution is probed at sampling points distributed uniformly in the space of parameters of interest. Having defined a metric in that space, the value of the distribution at a given point is obtained by accumulating the areas of the reconstructed mesh segments, whose associated parameters are within an assumed distance from that point. Afterwards, the values are divided by the volume centered at the probing point and restricted by the selected radius in order to express them in the conventional units, *i.e.*, using MRD.

For GBPDs, the probing space is composed of vectors ending at points lying on a unit sphere and starting at its center. The distance between boundary normals and the sampling directions is defined as the angle between these vectors. In this study, the limiting radius $\varrho_p = 7^\circ$ was used and was imposed by the resolution for determining boundary plane inclinations.[26] Because of crystal symmetries, each boundary plane has up to $4n_C$ equivalent normal vectors, and the distance is minimized over all of them; n_C stands for the number of symmetry rotations. It is enough to compute the distribution for directions from the standard stereographic triangle, since the remaining pieces of the function can be generated using the symmetry operators. The normalization factor is $An_C/4\pi$, with A being the area of the spherical cap restricted by ϱ_p.

Relative statistical errors of the distribution can be estimated as $1/\sqrt{nVf}$ with n being the number of boundaries (not mesh segments!) in the neighborhood of a sampling point and f being the value of the distribution at that point. All distributions shown below were computed using GBToolbox[27] and plotted using the GBContourPlot library.[28]

The GBPDs for the combined datasets are shown in Figure 2. Boundary data corresponding to the same material (*i.e.*, the same sintering temperatures and times) were joined in order to ensure better statistical reliability. A common pattern for the obtained distributions is the excess of near-(001) planes and deficiency of near-(111) planes. Values above (below) 1 MRD are read as over-representation (or under-representation) of corresponding planes compared to random boundaries. This anisotropy is the most visible for YSZ sintered for 20 hours at 1550 °C, where the height of the maximum at (001) is 1.95 ± 0.05 MRD. Relatively high peaks at this location are observed for 1500 °C-20 hours and 1600 °C-20 hours. Their heights are 1.44 ± 0.04 and 1.58 ± 0.07 MRD, respectively. For the remaining samples, the anisotropy is weaker—the distribution values at (001) range from 1.06 to 1.21 MRD. The values of GBPDs at (001), along with their uncertainties

Table I. Catalog of the Collected Datasets with Their Basic Characteristics

Dataset	Number of Grains	Number of Grain Boundaries	Mean Grain Size (and Its Standard Deviation) [μm]	GBPD at (001) [MRD]
1400 °C-2 h-1a	4026	14292	1.1 (1.0)	1.07 ± 0.01
1400 °C-2 h-1b	4800	16330	1.2 (1.1)	1.11 ± 0.01
1400 °C-2 h-1c	1790	5461	1.2 (1.0)	1.35 ± 0.03
1400 °C-2 h-2a	5824	20774	1.2 (1.1)	1.05 ± 0.01
1400 °C-2 h-2b	2393	7649	1.2 (1.1)	1.06 ± 0.02
1400 °C-2 h (Combined)	18833	64506	1.2 (1.1)	1.11 ± 0.01
1450 °C-2 h-1	1866	8447	1.9 (1.3)	1.35 ± 0.02
1450 °C-2 h-2	744	3141	2.0 (1.4)	1.04 ± 0.03
1450 °C-2 h-3	2129	10229	2.0 (1.5)	1.17 ± 0.02
1450 °C-2 h-4	1455	7218	2.0 (1.4)	1.15 ± 0.02
1450 °C-2 h (Combined)	6194	29035	2.0 (1.4)	1.21 ± 0.01
1475 °C-2 h-1	611	2823	2.6 (1.7)	1.09 ± 0.03
1475 °C-2 h-2	1065	5306	2.5 (1.7)	1.13 ± 0.02
1475 °C-2 h-3	950	4827	2.5 (1.8)	1.16 ± 0.03
1475 °C-2 h (Combined)	2626	12956	2.5 (1.7)	1.07 ± 0.02
1500 °C-2 h-1	724	3216	1.8 (1.0)	1.03 ± 0.03
1500 °C-2 h-2a	449	1972	2.6 (1.5)	1.10 ± 0.04
1500 °C-2 h-2b	237	843	2.4 (1.6)	1.33 ± 0.07
1500 °C-2 h-3a	409	1674	2.0 (1.1)	1.08 ± 0.04
1500 °C-2 h-3b	211	623	2.3 (1.6)	0.95 ± 0.07
1500 °C-2 h-4	116	322	3.0 (2.2)	1.11 ± 0.10
1500 °C-2 h (Combined)	2146	8650	2.2 (1.2)	1.06 ± 0.02
1525 °C-2 h-1	390	2022	3.2 (2.0)	1.15 ± 0.04
1525 °C-2 h-2a	388	1992	3.2 (2.0)	1.06 ± 0.04
1525 °C-2 h-2b	97	341	3.2 (2.0)	1.23 ± 0.10
1525 °C-2 h-3	322	1628	3.5 (2.2)	1.17 ± 0.05
1525 °C-2 h-4	445	2365	3.5 (2.4)	1.20 ± 0.04
1525 °C-2 h-5	436	2235	2.4 (1.3)	1.08 ± 0.04
1525 °C-2 h (Combined)	2078	10583	3.2 (1.9)	1.10 ± 0.02
1550 °C-2 h-1	128	426	3.2 (1.6)	1.04 ± 0.08
1550 °C-2 h-2	205	948	3.4 (2.0)	1.28 ± 0.06
1550 °C-2 h-3	128	438	3.0 (1.6)	1.06 ± 0.08
1550 °C-2 h (Combined)	461	1812	3.2 (1.8)	1.11 ± 0.04
1450 °C-20 h-1	1523	7606	2.3 (1.7)	1.15 ± 0.02
1450 °C-20 h-2a	1147	5753	2.3 (1.7)	1.19 ± 0.02
1450 °C-20 h-2b	285	1007	2.2 (1.7)	1.12 ± 0.06
1450 °C-20 h-3a	643	2496	1.9 (1.5)	1.14 ± 0.04
1450 °C-20 h-3b	1433	6801	2.2 (1.6)	1.25 ± 0.02
1450 °C-20 h (Combined)	5031	23663	2.2 (1.7)	1.19 ± 0.01
1475 °C-20 h-1a	189	785	3.8 (2.2)	1.15 ± 0.06
1475 °C-20 h-1b	158	657	3.6 (2.4)	1.02 ± 0.07
1475 °C-20 h (Combined)	347	1442	3.7 (2.3)	1.13 ± 0.05
1500 °C-20 h-1	109	428	4.2 (1.8)	1.30 ± 0.09
1500 °C-20 h-2	131	504	3.8 (1.2)	1.31 ± 0.08
1500 °C-20 h-3	137	614	5.2 (2.7)	1.78 ± 0.09
1500 °C-20 h-4	159	733	5.0 (2.7)	1.32 ± 0.07
1500 °C-20 h (Combined)	536	2279	4.6 (2.0)	1.44 ± 0.04
1525 °C-20 h-1	138	634	3.9 (2.4)	1.08 ± 0.07
1525 °C-20 h-2	92	279	2.9 (1.1)	1.07 ± 0.10
1525 °C-20 h-3	182	827	3.7 (1.6)	1.11 ± 0.06
1525 °C-20 h-4	148	604	1.9 (0.9)	1.12 ± 0.06
1525 °C-20 h-5	195	921	4.5 (2.5)	1.38 ± 0.07
1525 °C-20 h (Combined)	755	3265	3.5 (1.5)	1.15 ± 0.03

Table I. continued

Dataset	Number of Grains	Number of Grain Boundaries	Mean Grain Size (and Its Standard Deviation) [μm]	GBPD at (001) [MRD]
1550 °C-20 h-1a	86	318	4.2 (1.9)	2.06 ± 0.13
1550 °C-20 h-1b	85	292	3.9 (1.9)	2.13 ± 0.14
1550 °C-20 h-2a	151	626	3.4 (1.3)	1.83 ± 0.09
1550 °C-20 h-2b	72	248	3.0 (1.5)	2.01 ± 0.15
1550 °C-20 h-3	189	789	3.6 (1.4)	1.92 ± 0.08
1550 °C-20 h (Combined)	583	2273	3.6 (1.5)	1.95 ± 0.05
1575 °C-20 h-1	35	116	7.0 (2.8)	1.52 ± 0.19
1575 °C-20 h-2	56	209	6.7 (3.6)	1.27 ± 0.13
1575 °C-20 h-3a	41	122	6.0 (2.9)	0.80 ± 0.14
1575 °C-20 h-3b	40	120	5.8 (2.5)	1.31 ± 0.17
1575 °C-20 h-4a	25	78	6.2 (2.9)	0.60 ± 0.15
1575 °C-20 h-4b	43	146	5.8 (4.6)	1.33 ± 0.16
1575 °C-20 h-5a	50	186	4.9 (1.4)	0.84 ± 0.11
1575 °C-20 h-5b	29	85	6.1 (1.7)	1.22 ± 0.20
1575 °C-20 h (Combined)	319	1062	6.2 (2.5)	1.16 ± 0.06
1600 °C-20 h-1	38	133	7.2 (3.4)	2.13 ± 0.21
1600 °C-20 h-2	54	205	6.6 (3.3)	1.51 ± 0.14
1600 °C-20 h-3	51	187	7.0 (3.8)	1.22 ± 0.14
1600 °C-20 h-4a	41	145	6.3 (2.9)	1.77 ± 0.18
1600 °C-20 h-4b	19	41	6.7 (3.1)	1.68 ± 0.34
1600 °C-20 h-5	31	106	7.4 (3.2)	1.76 ± 0.22
1600 °C-20 h-6	47	179	7.4 (3.3)	1.31 ± 0.14
1600 °C-20 h (Combined)	281	996	7.0 (3.3)	1.58 ± 0.07

Dataset names indicate sintering temperatures and times. Suffixes correspond to numbers of measurements for a given material; the presence of additional letters means that the dataset was split into subsets during post-processing

for all joint datasets, are collected in Figure 3. This graph reveals no obvious correlation between the anisotropy of boundary plane parameters and sintering temperature. We might, however, say that, on average, the anisotropy is stronger for samples sintered for 20 hours compared to those processed for 2 hours. Besides that, the outliers with the highest anisotropy correspond to the samples sintered for 20 hours in the temperatures equal or greater than 1500 °C.

As a cross-validation, partial GBPDs for all subsets were calculated, too. Elevated values near the (001) pole are seen for majority of partial distributions as well. GBPD values at (001) for all subsets are listed in Table I. Some variations between samples collected from the same material are apparent. For instance, Figure 4 shows partial distributions for samples sintered for 20 hours at 1525 °C. This is an example with mild deviations between subsets. A quite sharp maximum at (001) with the height 1.38 ± 0.07 MRD is seen for subset 1525 °C-20 h-5. Weaker peaks of 1.11 and 1.12 MRD are present at this location for 1525 °C-20 h-3 and 1525 °C-20 h-4, respectively, and they exceed 1 MRD by about 2σ (with σ denoting the corresponding errors). Finally, for 1525 °C-20 h-1 and 1525 °C-20 h-2, 1 MRD is within about 1σ, and no clear peaks are distinguishable. Merging the subsets together results in the value of 1.15 ± 0.03 MRD at (100).

Another interesting example of partial distributions is those obtained for the sample sintered for 20 hours at 1550 °C (Figure 5). We can see that all subsets exhibit relatively strong anisotropy, the (001) peak reaches from 1.83 to 2.13 MRD, and is always far more than 3σ above 1 MRD. This confirms that such anisotropy is the true feature of that material (we generally follow the criterion to have at least 3σ above the level of the random distribution to claim over-representation of given boundary planes).

On the opposite pole, the largest fluctuations in GBPD between the subsets are observed for two materials with the largest grains: 1575 °C-20 hours and 1600 °C-20 hours. The values of GBPD at (001) range from 0.6 to 1.52 MRD and from 1.31 to 2.13 MRD, respectively. The larger the grains, the smaller the number of grains (and grain boundaries) that can be packed into a comparable volume. Thus, statistical reliability of these subsets is lower compared to data gathered for the other sinters. This is reflected in relatively high errors of GBPD for the subsets of 1575 °C-20 hours and 1600 °C-20 hours. For these materials, it was crucial to combine the subsets in order to reduce the uncertainties. Nevertheless, it appears that the levels around which GBPDs at (100) oscillate are very different for these two materials. For the merged datasets, the levels are 1.16 ± 0.06 and 1.58 ± 0.07 MRD for 1575 °C-20 hours and 1600 °C-20 hours, respectively. In the former case, the value is almost 3

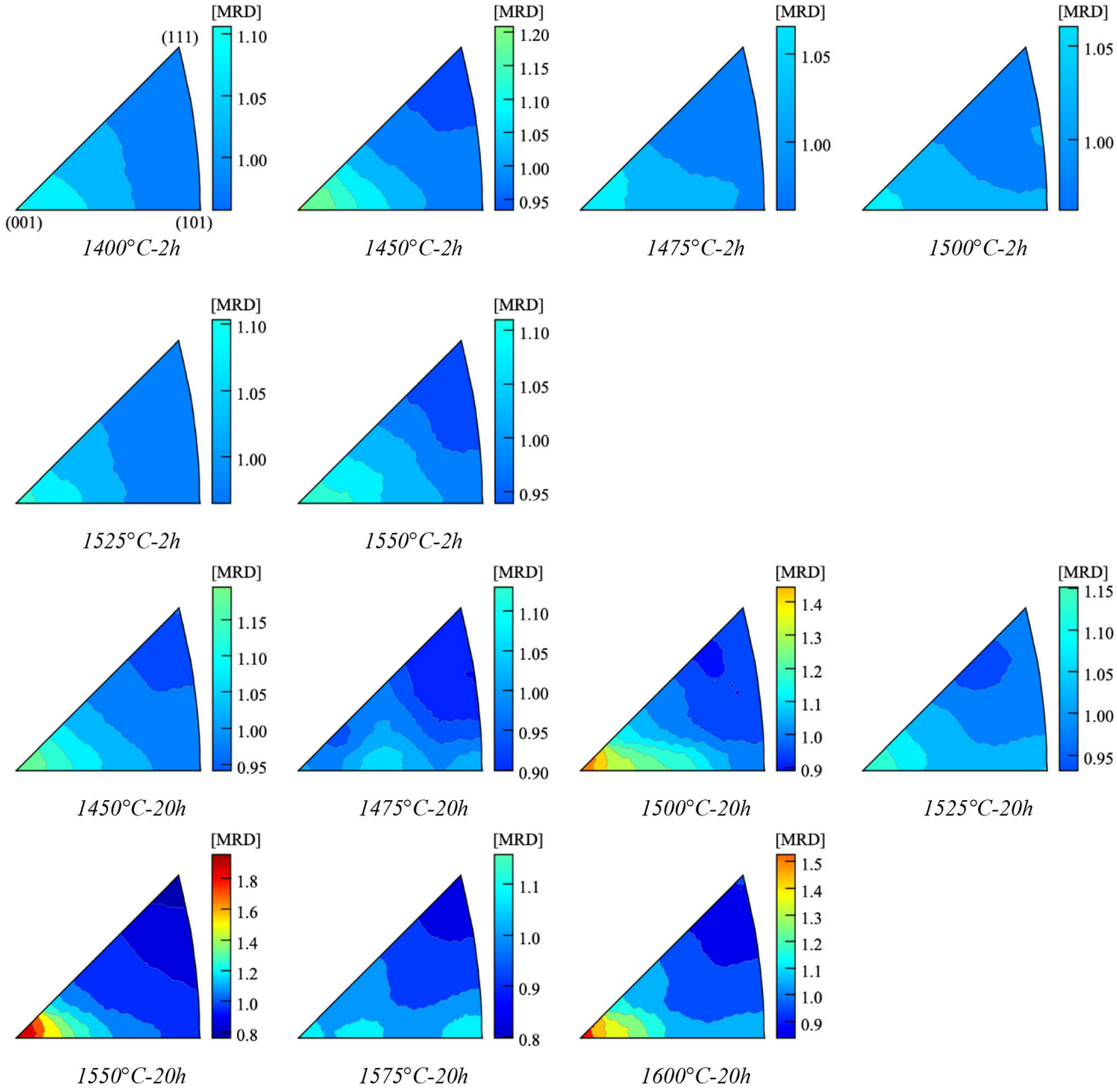

Fig. 2—Grain boundary plane distributions (independent of misorientations) for all investigated YSZ sinters. Only the combined datasets are taken into consideration. Distributions are plotted in the standard stereographic triangle for the cubic crystal symmetry. Units are multiples of the random distribution.

σ away from 1 MRD, while for the latter—it is far more than 3σ.

These observations were supported by the X-ray diffraction measurements carried out using the HZG beamline (P07B) located at PETRA III DESY, Hamburg, Germany.

The textures of the cubic phase of samples sintered at *1500 °C-20 h, 1550 °C-20 h, 1575 °C-20 h*, and *1600 °C-20 h* are presented in Fig 6. As can be seen, all of them are very weak exhibiting mainly the so-called cube component $\{001\} < 100 >$ with a maximum of 1.25 MRD. However, the strongest texture can be detected for the sample sintered at 1550 °C. This is in line with grain boundary analysis where the value of the GBPD at (001) reached the maximum. The second strongest texture has been measured for the sample sintered at 1500 °C. The two other samples are characterized practically by random texture with marginal cube components. A thorough analysis of (111) PFs shows also disfavor of near-(111) planes with respect to the sample coordinate system (CS, TD_1, TD_2)

Another microstructure characteristic with crystallography of grain boundaries in the background is the frequencies of occurrence of geometrically characteristic boundaries. To recall, based on the five macroscopic boundary parameters, several special boundary

geometries are distinguishable. A twist (tilt) grain boundary has at least one representation, where the misorientation axis is orthogonal (parallel) to the boundary plane. Symmetric (180 deg-tilt) boundaries are twist (tilt) boundaries, whose misorientations are rotations by 180 deg. To check if a given boundary is twisted, one can calculate the α_N parameter defined as the angle—minimized overall equivalent boundary representations—between the misorientation axis and the normal to the boundary.[29] Analogous parameters α_S and α_I were defined for symmetric and 180 deg—tilt boundaries, respectively.[30] If the parameter is below a certain threshold, then the boundary can be classified to the corresponding group. There exists a similar parameter for tilt boundaries, too, but current experimental capabilities do not allow to derive tilt from random boundaries for materials of cubic symmetry. The area fractions of twist, symmetric, and 180 deg-tilt boundaries for the investigated samples are collected in Figure 7 and compared with the percentages among random grain boundaries; the threshold of 8° was assumed as approximation of the measurement resolution (it takes into account accuracy of determining both misorientations and boundary inclinations).[26] The uncertainties σ were estimated using relative errors $1/\sqrt{N}$, where N is the number of boundaries falling into the considered group. It turns out that the largest deviations from random boundaries occur for symmetric boundaries; for the datasets with the largest numbers of boundaries (1400 °C-2 hours, 1450 °C-2 hours, 1475 °C-2 hours, 1450 °C-20 hours), the over-representation exceeds 3σ. The percentages for twist boundaries in YSZ are very close to those for random boundaries. For 180° tilts, slight divergence is observed for some samples.

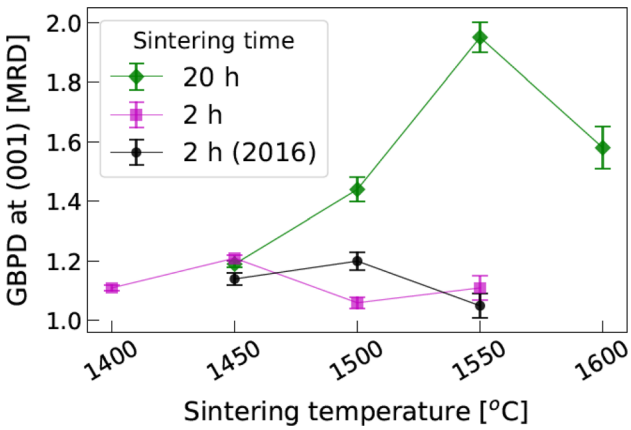

Fig. 3—Values (in multiples of the random distribution) of grain boundary plane distributions at (001) pole for all YSZ sinters. The results of this report (green and magenta) are compared to those of Ref. 10 (black) (Color figure online).

Apart from crystallography of grain faces, 3D data allow for studying topology of the microstructure. One of the topological aspects of microstructures is the distribution of the number of faces per grain. Figure 8 shows such distributions for two materials sintered for 2 hours at 1400 °C and 1475 °C 2 hours. The former is built of the smallest grains among all the investigated samples (mean diameter is equal 1.2 μm), the latter is composed of grains of medium-size (compared to other

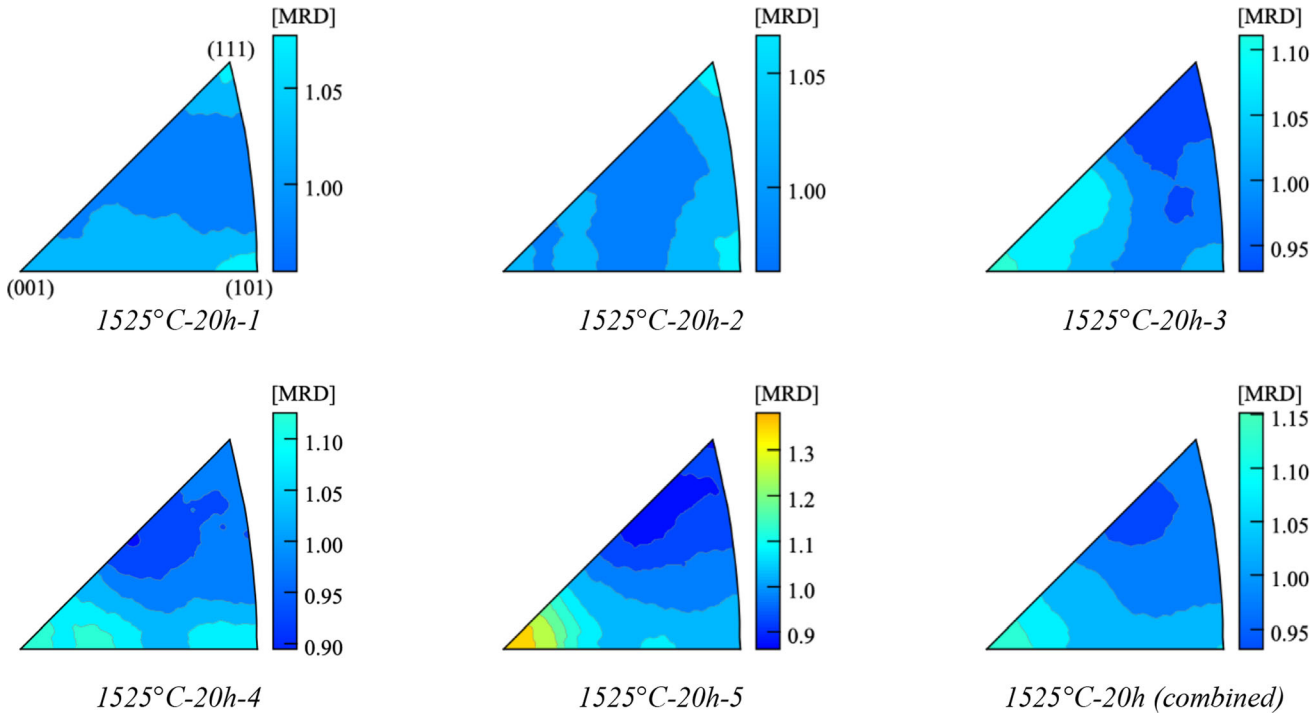

Fig. 4—Distributions of grain boundary planes for all subsets collected from YSZ sintered at 1525 °C for 20 hours, plus for the combined dataset. Distributions are given in multiples of the random distribution and displayed in the standard stereographic triangle.

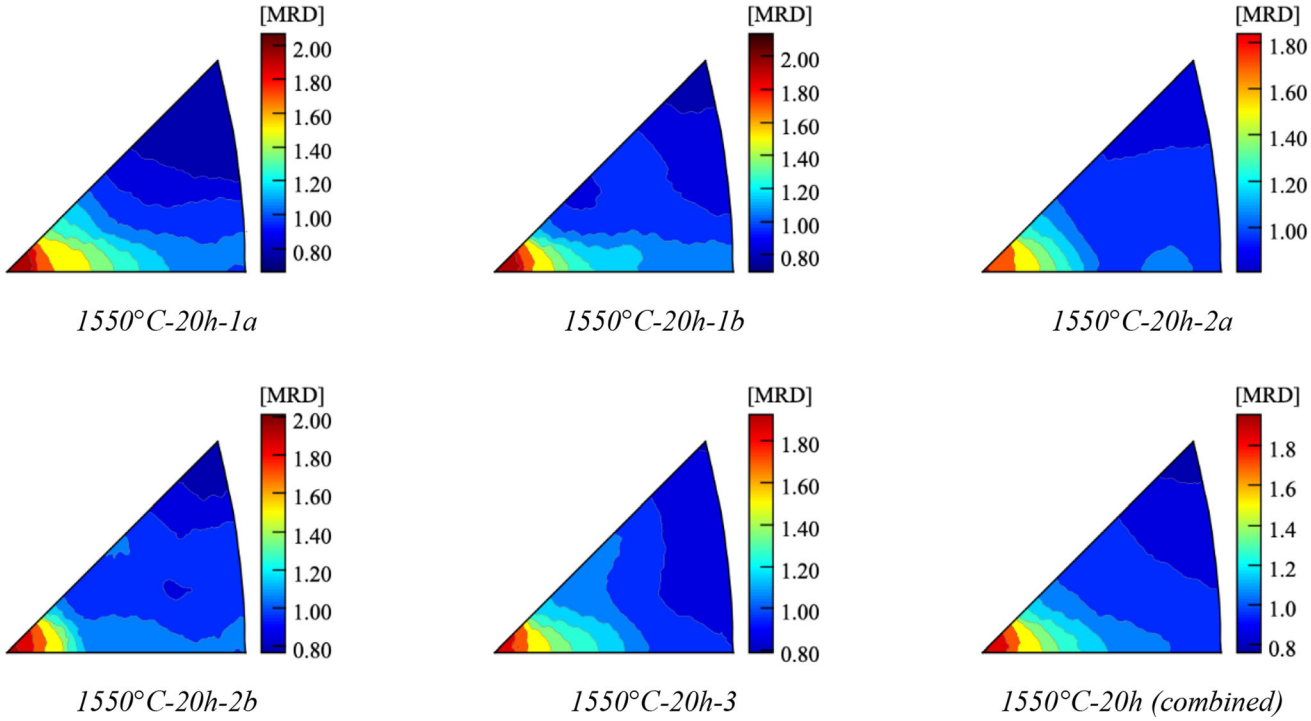

Fig. 5—Grain boundary plane distributions for all samples collected from YSZ sintered at 1550 ºC for 20 h and the combined data. Functions are plotted in stereographic projection and expressed in multiples of the random distribution.

studied materials) with mean diameter of 2.5 μm The shapes of these distributions are similar, but the mean numbers of faces per grain are slightly different, respectively, 12.7 and 11.5. For this and below analyses, only the grains fully contained in the 3D maps are included; those cut by the outer surfaces of the maps were excluded in order to avoid bias. This prerequisite unfortunately reduces the number of useful grains in a dataset, and in consequence, such analysis is possible only for samples with relatively small grains where interior of the 3D map still contains many grains (*e.g.,* Figures 1(a) and (b)). In the maps collected from large-grain materials, high fractions of grains lie on the outer surfaces and the number of remaining grains is insufficient for reliable investigations (*e.g.*, Figures 1(c) and (d)).

Figure 9 presents the probabilities of occurrence of grains as a function of their size and number of faces for three YSZ sinters: the two which are considered above and the one sintered for 20 h at 1450 °C with a mean grain size of 2.2 μm. A linear correlation between the number of faces per grain and grain diameter expressed as multiples of the mean grain diameter (for a given sample) is clearly seen. The corresponding Pearson correlation coefficients are 0.88, 0.89, and 0.92 for *1400 °C-2 h*, *1475 °C-2 h*, and *1450 °C-20 h*, respectively. The graphs for the latter two datasets are very similar. Compared to those two, the first one looks like it was cropped. The cut-off at about 0.5 times the mean grain diameter is related to the minimum number of voxels needed to form a grain. With the mean diameter of 1.2 μm, voxels being cubes with edges 0.2 micron long, and the requirement of at least 20 voxels, there are no grains smaller than 0.5 times the mean diameter in the data. Nevertheless, the correlation between the grain size and number of faces per grain is observed for all samples. Similar correlation was observed earlier for titanium[13] and brass.[15]

IV. DISCUSSION

Let us first comment on the obtained GBPDs. This piece of analysis is essentially an extension of the initial studies carried out in Reference 10. Previously, three YSZ samples were investigated; they had been sintered for 2 h at 1450 °C, 1500 °C, and 1550 °C. For each of those samples, a relatively small peak at the (001) pole and a valley at (111) were observed. The heights of maxima at (001) ranged from 1.05 to 1.27 MRD. No relationship between the peak height and sintering temperature was claimed. In this work, we have had far more samples at our disposal, sintered in the range of temperatures from 1400 °C to 1600 °C and for two different times, mainly 2 and 20 hours. In order to allow direct comparison with the past result, the GBPDs for all new samples were computed utilizing the same KDE-based approach. Also, as in Reference 10, the same limiting distance, $\varrho_p = 7°$, was set. The new results indicate a similar preference for near-(001) planes and disfavor of near-(111) planes. The height of the (001) maximum is low in most cases—for 10 out of 13 samples, it varies from 1.06 to 1.21 MRD. Such heights fall into the same range as in the earlier study. The peak heights obtained in this and the previous work are compared in Figure 3. For materials sintered for 2 hours, the peak heights seem not to be influenced much by the

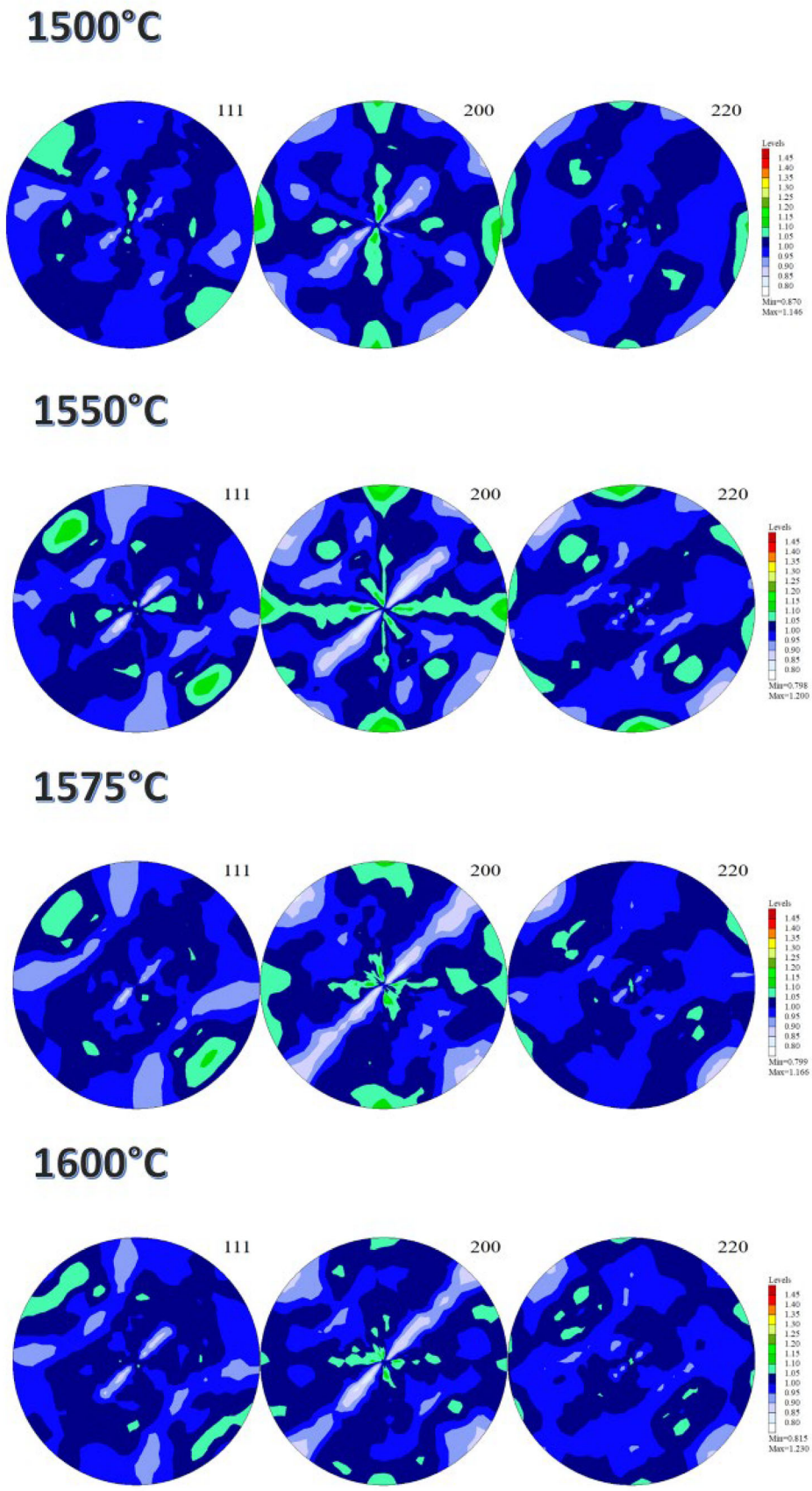

Fig. 6—X-ray measurement of the global texture in the samples *1500 °C-20 h, 1550 °C-20 h, 1575 °C-20 h*, and *1600 °C-20 h*.

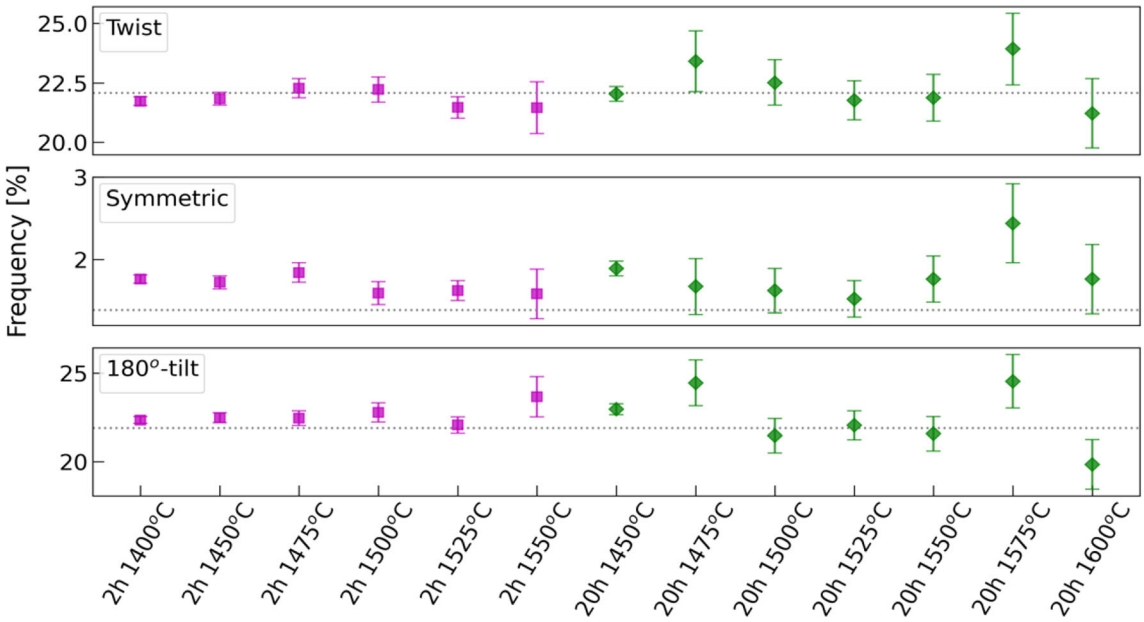

Fig. 7—Frequencies of occurrence of twist, symmetric, and 180 deg-tilt grain boundaries in the investigated samples; the frequencies were computed for the combined datasets assuming the threshold of 8 deg. Dotted horizontal lines correspond to the frequencies among random boundaries.

sintering temperature. However, for samples sintered for 20 hours, there are three outliers. The heights for datasets *1500 °C-20 h*, *1550 °C-20 h*, and *1600 °C-20 h* are 1.44, 1.95, and 1.58 MRD, respectively. Figure 10 shows the heights of the peak at (001) as a function of grain size. It appears that the outliers correspond to mean diameters greater than 3.6 μm. All samples sintered for 2 hours have mean grain sizes smaller than this value. Obviously, longer sintering led to grain growth. It is, however, not clear why the highest anisotropy (which is observed consistently across all subsets) is observed for *1550 °C-20 h*—in this case neither the sintering temperature was the highest (among the investigated samples) nor the resulting grains are the largest. Based on our data, we might say that the presence of large grains (with mean diameter > 3.6 μm) is a necessary condition for stronger anisotropy to occur. One of the possible reasons is the strongest $\{001\} < 100 >$ texture observed in this sample. Nonetheless, the question remains of what is the mechanism responsible for both preferred orientations of grains and their GBPDs at *1550 °C-20 h*.

In the previous paper,[10] also initial estimates for percentages of geometrically characteristic boundaries were reported. There were some premises that symmetric boundaries may be over-represented compared to random boundaries. However, the deviation from the level corresponding to random boundaries was too little, *i.e.*, at most 2σ only. This study provides stronger proofs. For 4 datasets with the highest cardinality, the fraction of symmetric boundaries for the YSZ exceeds that for random boundaries by more than 3σ. Moreover, 3σ excess of symmetric boundaries is observed for sinters processed for 2 hours as well as for 20 hours. Hence, the mild over-representation of symmetric boundaries is likely the feature of YSZ. Moreover, among smaller datasets, there are 3 samples with 2σ over-representation of symmetric boundaries. From sample to sample, the amount of twist boundaries in the YSZ generally fluctuates no further than about 1σ from that corresponding to random boundaries; the level close to 2σ is observed for one sample only. Thus, it is hard to tell whether twist boundaries are preferred in any way in zirconia. Regarding 180 deg-tilt boundaries, we have 3 samples with about 2σ and one with about 3σ divergence from random boundaries. Thus, there are some premises that 180 deg-tilts might be favored in some way, but to confirm this, more accurate data would be still required. In the 5D grain boundary distribution for YSZ studied in Reference [18] and its approximation obtained via stereology,[31] the most significant peaks correspond to symmetric boundaries (*e.g.*, of $\Sigma 3$ misorientation and the (111) boundary plane, $\Sigma 11/(1\bar{1}3)$, and a few more boundaries with misorientations about the [110] axis) which is consistent with the increased percentage of symmetric boundaries. On the other hand, these peaks correspond simultaneously to twist and 180 deg-tilt boundaries, but this is not reflected in the relevant fractions. A possible explanation is that symmetric boundaries are very rare among random boundaries (1.4 pct) compared to twists (22 pct) and 180 deg-tilts (21.9 pct). The same contribution may lead to fraction of symmetric boundaries very different (relatively) from the one for random boundaries, while its impact on (already quite high) percentages of twist and 180 deg-tilt boundaries may be overlooked.

Let us move to topological aspects of zirconia microstructure. We are aware of several analyses concerning the number of faces per grain.[13] Although these analyses were done for metals, the shapes of the distributions of probabilities of occurrence of grains with a given

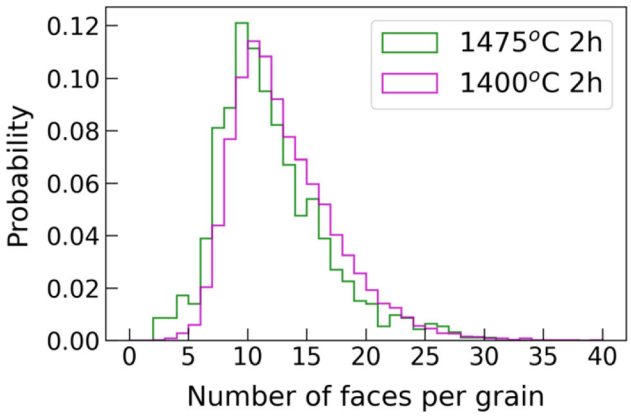

Fig. 8—Distribution of the number of faces per grain for two of the studied sinters.

number of faces are similar to that obtained for YSZ. The mean number of faces per grain obtained for zirconia (*i.e.*, 11.5 to 12.7) is similar to that for brass (11.1 to 11.8),[15] AlSn (12.5),[17] and iron (12.1 to 12.2),[16] but smaller compared to that for titanium, *i.e.*, from 13.7[14] to 14.2.[13] Interestingly, for titanium similar mean values were obtained for both hexagonal close-packed and body-centered cubic phases, indicating independence of this topological parameter from crystal structure. In the aforementioned studies, also the maximum numbers of faces per grain were reported. For instance, for titanium, the values 40[14] and 70[13] were given. In the latter case, it is, however, clear that rare grains with more than 40 faces contribute to a long tail of the distribution of the probability of finding a grain with certain number of faces. Moreover, existence of such outliers is affected by the reconstruction and clean-up procedures.[13] Similarly for zirconia, we found grains having up to about 60 faces for *1450 °C-2 h*, but non-negligible contributions to the distribution are up to about 30 faces only. In contrast, the maximum number of faces per grain reported for brass and AlSn were 20 and 23 only, respectively, but these results were obtained using very different methodology: (a limited number of) grains used in the analysis were physically separated from a material.

V. CONCLUSIONS

A large set of 3D orientation maps for the YSZ samples was collected utilizing 3D EBSD technique. This is probably the largest collection of this type registered for zirconia and the most diverse in terms of sintering time and temperature, and consequently, grain size. These data were used for investigation of anisotropy in grain boundary plane parameters, frequencies of occurrence of geometrically characteristic boundaries, and number of faces per grain.

A common observation for all GBPDs is under-representation of near-(111) planes and over-representation of near-(001) planes (compared to random boundaries). For most of the YSZ samples, this anisotropy is mild, reaching at most about 1.2 MRD. However, some exceptions were seen, too. For 3 out of 13 samples, the

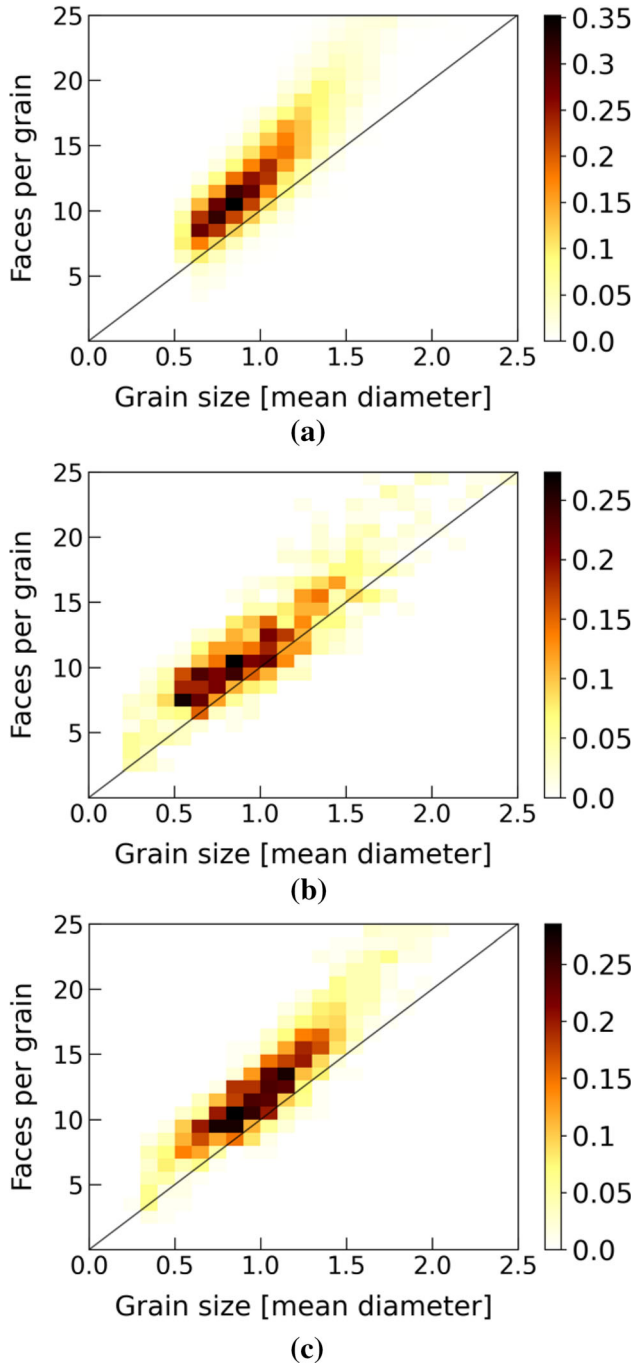

Fig. 9—Probabilities of occurrence as a function of the number of grain faces and the grain size given in multiples of the mean grain diameter for (*a*) *1400 °C-2 h*, (*b*) *1475 °C-2 h*, and (*c*) *1450 °C-20 h*. The diagonal line given as $y = 10x$ is for reference only.

anisotropy was stronger. The highest peak, close to 2 MRD, was observed for zirconia sintered for 20 hours at 1550 °C. The strong anisotropy occurred for samples built of the largest (on average) grains, but large grains themselves are not sufficient condition for observing strong anisotropy. We have collected enough evidences to say that symmetric boundaries are slightly more frequent in zirconia compared to random boundaries. It can be confirmed that there are premises for mild

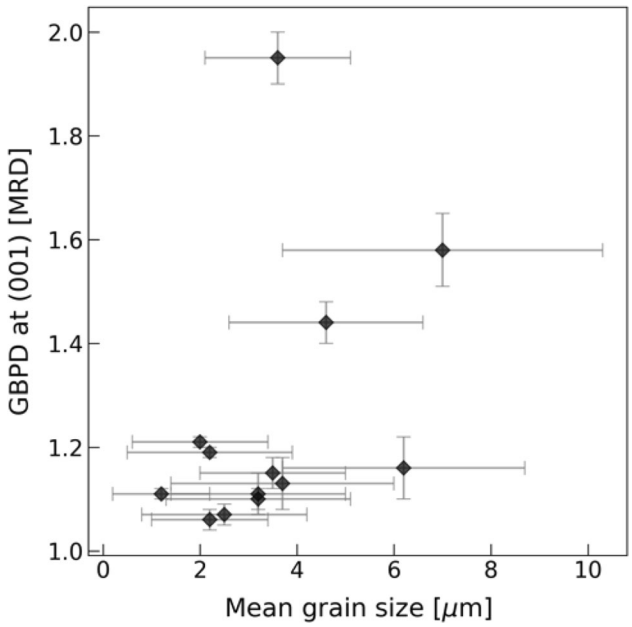

Fig. 10—Values (in multiples of the random distribution) of grain boundary plane distributions at (001) pole as a function of mean grain size, cf. Figure 3.

over-representation of 180 deg-tilt boundaries; however, the evidence is still too weak. Based on the current data, twist boundaries do not occur more frequent than among random boundaries.

The topological characteristics like distribution of the number of faces per grain and mean number of faces per grain obtained for the YSZ are similar to those known for metals. The same (as for metals) close-to-linear correlation between the number of faces and grain size is seen for the YSZ.

Summarizing, the impact of processing history of the YSZ samples on microstructure topology and amount of geometrically characteristic boundaries turns out to be subtle. It is more apparent in GBPDs; thus, only the latter seem to be a potential tool for process monitoring of this material.

ACKNOWLEDGMENTS

The work was supported by the Polish National Science Centre upon decision DEC- 2017/27/B/ST8/00143. The SEM/FIB/EBSD studies were performed in the Accredited Testing Laboratories at the Institute of Metallurgy and Materials Science of the Polish Academy of Sciences.

AUTHOR CONTRIBUTIONS

MF: 3D EBSD experiments, formal analysis, writing—review and editing. KG: Simulation and calculations of 3D data, writing—original draft. RCh: X-ray diffraction measurements. ZP: Manufacturing and sintering of all YSZ samples.

CONFLICT OF INTEREST

On behalf of all authors, the corresponding author states that there is no conflict of interest.

OPEN ACCESS

REFERENCES

1. O. Yamamoto: *Electrochem. Acta*, 2000, vol. 45, pp. 2423–35.
2. W. Zhu and S. Deevi: *Mater. Sci. Eng.*, 2003, vol. 362A, pp. 228–39.
3. X. Weng, D. Brett, V. Yufit, P. Shearing, N. Brandon, M. Reece, H. Yan, C. Tighe, and J. Darr: *Solid State Ionics*, 2010, vol. 181, pp. 827–34.
4. S. Kim: *Scripta Mater.*, 2011, vol. 65, pp. 65–66.
5. A.H. Heuer, N. Claussen, W.M. Kriven, and M. Rühle: *J. Am. Ceram. Soc.*, 1982, vol. 65, pp. 642–50.
6. J. Abriata, J. Garces, and R. Versaci: *Bull. Alloys Phase Diagr.*, 1986, vol. 7, pp. 116–23.
7. F. Gallino, C. Di Valentin, and G. Pacchionia: *Phys. Chem. Chem. Phys.*, 2011, vol. 13, pp. 17667–75.
8. H.Y. Chen, H.C. Yu, J. Cronin, J. Wilson, S. Barnett, and K. Thornton: *J. Power Sources*, 2011, vol. 196, pp. 1333–37.
9. L. Helmick, S. Dillon, K. Gerdes, R. Gemmen, G.S. Rohrer, S. Seetharaman, and P.A. Salvador: *Int. J. Appl. Ceram. Tec.*, 2011, vol. 8, pp. 1218–28.
10. P. Bobrowski, M. Faryna, and K. Głowiński: *Mater. Charact.*, 2016, vol. 122, pp. 137–41.
11. K. Głowiński and A. Morawiec: *Metall. Mater. Trans. A*, 2014, vol. 45A, pp. 3189–94.
12. V. Randle: *Mater. Sci. Tech.*, 2010, vol. 26, pp. 253–60.
13. M.N. Kelly, K. Głowiński, N.T. Nuhfer, and G.S. Rohrer: *Acta Mater.*, 2016, vol. 111, pp. 22–30.
14. D.J. Rowenhorst, A.C. Lewis, and G. Spanos: *Acta Mater.*, 2010, vol. 58, pp. 5511–19.
15. F.C. Hull: *Mater. Sci. Tech.*, 2013, vol. 4, pp. 778–85.
16. C. Zhang, M. Enomoto, A. Suzuki, and T. Ishimaru: *Metall. Mater. Trans. A*, 2004, vol. 35A, pp. 1927–33.
17. M. Williams and C.S. Smith: *Trans. AIME*, 1952, vol. 194, pp. 755–65.
18. M. Faryna and K. Głowinski: *Acta Mater.*, 2022, vol. 226, pp. 117606–17.
19. A. Wójcik, R. Chulist, P. Czaja, M. Kowalczyk, P. Zackiewicz, N. Schell, and W. Maziarz: *Acta Mater.*, 2021, vol. 219, pp. 117237–47.
20. R. Chulist and P. Czaja: *Scripta Mater.*, 2020, vol. 189, pp. 106–11.
21. K. Pawlik: *Phys. Stat. Sol. (b)*, 1986, vol. 134, pp. 477–83.

22. H.J. Bunge: *Texture Analysis in Materials Science*, Cuvillier Verlag, Göttingen, 1993, pp. 4–8.
23. M.A. Groeber and M.A. Jackson: *Integrating Materials and Manufacturing Innovation*, 2014, vol. 3, pp. 56–72.
24. J. Ahrens, B. Geveci, and Ch. Law: *ParaView: An End-User Tool for Large Data Visualization, Visualization Handbook*, Elsevier, 2005.
25. A. Morawiec: *J. Appl. Cryst*., 2009, vol. 42, pp. 783–92.
26. D.M. Saylor, A. Morawiec, and G.S. Rohrer: *Acta Mater*., 2003, vol. 51, pp. 3663–74.
27. K. Głowiński, A. Morawiec: *Proceedings of the 3D Materials Science*, 2012, pp. 119-24.
28. K. Głowiński: *GBContourPlot* , 2020, https://github.com/kglowins/gbcontourplot.
29. A. Morawiec and K. Głowiński: *Acta Mater*., 2013, vol. 61, pp. 5756–67.
30. K. Głowiński: *J. Appl. Cryst*., 2014, vol. 47, pp. 726–31.
31. M.K. Kini: *Philos. Mag*., 2018, vol. 98, pp. 1865–83.